The Relationship between Upper-Ocean Variability and the Madden-Julian Oscillation in Extended-Range Simulations

Xiaodong Hong, Carolyn A. Reynolds, James D. Doyle
Marine Meteorology Division
Naval Research Laboratory
Monterey, CA 93943

Paul May
Computer Science Corporation
Monterey, CA 93943

Abstract— **The relationship between upper-ocean variability and the Madden-Julian Oscillation in extended-range simulations is examined using the Navy's non-hydrostatic COAMPS regional modeling system in a two-way coupled mode for the Dynamics of the Madden Julian Oscillation field experiment period (DYNAMO) during November to December 2011. Results show the simulation better captures the initiation, propagation and characteristics of the MJOs when the model horizontal resolution is increased from 45 km to 27 km. Variation of SST in time is in phase with surface heat flux, in which SST warms (cools) during the suppressed (active) phase through strong downward (upward) heat flux. Barrier layers that exist during the suppressed phase and erod during the active phase are consistent between the observation and the 27-km run. The extended-range simulations simulate the propagation of oceanic downwelling equatorial Rossby waves, which provide favorable conditions for convective activity for initiation of the MJO. The model simulations are also able to capture the diurnal warming during the suppressed phase.**

Keywords—coupled air-ocean extended-range simulations; the Madden-Julian Oscillation (MJO); Air-ocean interaction; upper-ocean variability

I. Introduction

Regional extended-range forecasting would be very useful for protecting life and property from damage due to severe weather. However, model extended-range simulations with high horizontal resolution are computationally expensive. In the tropics, the primary component of intraseasonal variability is the Madden-Julian oscillation (MJO) [1], which generally propagates eastward at 5 m s^{-1} with a period of 30-60 days [2]. To evaluate the capability of a regional mesoscale air-ocean coupled modeling system in simulating the MJO in the extended-range given current computational resources, we have tested two different horizontal resolutions using a large domain size. Results from two different model runs are compared with the observation and discussed to examine the impact of horizontal resolution on the regional extended-range simulations. The paper also reveals the relationship between upper-ocean variability and the MJO in regional extended-range simulations.

II. Model and Data

A. Two-way coupled system and model configuration

The regional two-way air-ocean coupled system used in this study includes the U.S. Navy's Coupled Ocean/Atmosphere Mesoscale Prediction System (COAMPS®) for the atmospheric component [3] and the U.S. Navy's Coastal Ocean Model (NCOM) for the oceanic component [4]. The atmospheric component provides a total of six ocean surface boundary forcing fields to the ocean component, while the ocean model provides a new sea surface temperature to the atmosphere that influences the next time step prediction of the atmospheric surface fluxes and wind stress. These forcing fields include the sea level pressure, the surface wind stress in the east-west and north-south directions, the total heat and moisture fluxes and the net solar radiation.

Initial conditions for the atmospheric component are from a COAMPS multivariate optimal interpolation analysis with the first guess fields from NOGAPS analyses used as a background for the analyses of the available observations. The 1/8^{o} global NCOM analyses are used to start NCOM. NOGAPS 1^{o} × 1^{o} analyses are also used for atmospheric lateral boundary conditions (LBCs), while for the oceanic component the global NCOM analysis and daily 24-forecast are utilized. Both atmospheric and oceanic lateral boundary conditions are updated at a 6 h frequency. It should be noted that for a real-time prediction mode, the use of global analysis fields or composites of forecast fields derived from many shorter time periods (as from global NCOM) for LBCs is not possible. Therefore, extended-range global forecasts from both atmosphere and ocean or from global coupled atmosphere-ocean forecasts will be needed for real time regional extended-range forecasts.

Fig. 1. Domain size, terrain height (brown) and ocean bathymetry (blue). Units are meters.

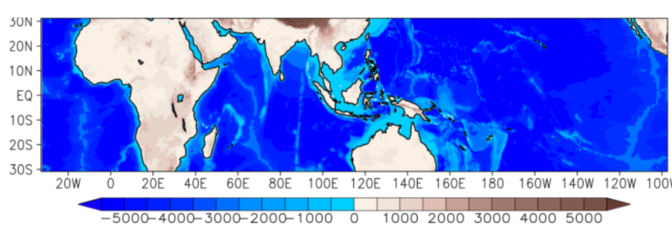

The SST for the atmospheric model for the two experiments is the same initially and provided by the Navy Coupled Ocean Data Assimilation (NCODA), which uses a

COAMPS® is a registered trademark of the Naval Research Laboratory three-dimensional variational data assimilation scheme [5]. The starting date-time-group for both experiments is 00 UTC 31 October 2011 and simulation length is two months through 21 UTC 31 December 2011.

B. Data used for model verification

The Tropical Rainfall Measuring Mission multi-satellite precipitation analysis (TRMM product 3B42) [6] is used for verifying model precipitation. The European Centre for Medium-Range Weather Forecasts (ECMWF) deterministic forecast model analysis data on pressure levels and the surface in GRIB1 format at 6-hourly 0.25^o resolution are used for verifying wind and SST. In situ data located at 0^o, 80.5^{o}E from Research Moored Array for African-Asian-Australian Monsoon Analysis and Precipitation (RAMA) program [7] are used to evaluate surface wind and ocean temperature, salinity and current.

III. RESULTS

A. MJO precipitation

Time-longitude Hovmöller diagrams of precipitation from the TRMM 3B42 and the two model forecasts are displayed in Fig. 2a-c, respectively. The TRMM observation indicates three MJO episodes depicted as MJO1, MJO2 and MJO3 (i.e., the first, second and third events of DYNAMO) [8][9] in Fig. 2a. The forecast time period contains MJO2 in its entirety. The other two MJO episodes are partially included, with the last stage of MJO1 and most portions of MJO3 contained within the forecast period. The model forecast from 45-km run (Fig. 2b) shows a reasonable similarity to the TRMM (Fig. 2a) for MJO1 and the early stage of MJO2. However, the eastward propagation of MJO2 is blocked over the Maritime Continent.

Fig. 2. Hovmöller diagrams of 3-h precipitation (mm day^{-1}) from (a) TRMM 3B42, (b) 45-km run and (c) 27-km run. All are averaged between 5^{o}S and 5^{o}N.

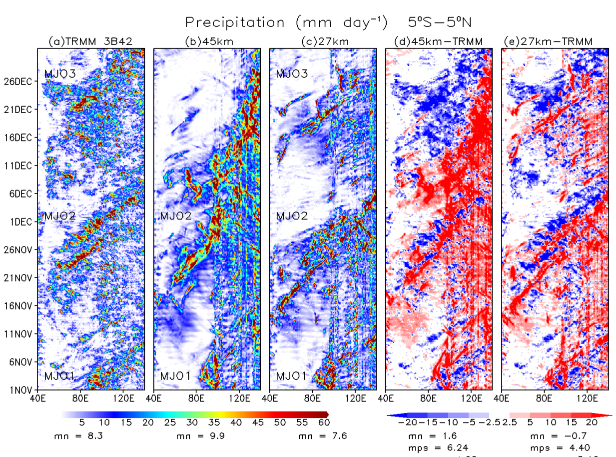

This is a common problem in model predictions due to errors in representing the scale interactions between the propagating MJO and complex topography, which leads to local errors in latent heat release in modeling systems [10]. This blocking with excessive amounts of precipitation extends until late December. Furthermore, MJO3 is missing in 45-km run, which instead exhibits a dry period from 12 December to the end of December between 40 and 100^{o}E. In contrast to the 45-km run, 27-km run (Fig. 2c) provides significantly improved results for the three MJOs, especially considering that MJO2 and MJO3 occur 20 and 40 days into the simulation, respectively. Although the timing for MJO2 in 27-km run appears earlier than observed, the mean precipitation in the time-longitude area has less bias than for 45-km run. Over-estimation of precipitation for MJO2 and the lack of a well-defined MJO3 results in large mean positive (6.24 mm day^{-1}) and negative biases (-4.6 mm day^{-1}) in 45-km run (Fig. 2d) during those time periods. The overall mean bias in 27-km run is small (-0.7 mm day^{-1}) due to small difference between positive and negative biases, which are due to errors in the timing of the MJOs (Fig. 2e).

B. Surface characteristics

COAMPS model output is compared with in situ data from the RAMA (0^o, 80.5^{o}E). Model simulations are able to capture the characteristics of the MJO as shown from the observation. Since the simulations cover the whole period of MJO2, we will focus on discussion of MJO2. During the suppressed phase from Nov 12 to 22, wind speeds are small (Fig. 3a and 3b) and air temperature is warm (Fig. 3c) due to strong short wave radiation (Fig. 3f). Moisture is building up during this phase (Fig. 3d) and sea-level pressure decreases (Fig. 3e) when convection is more active. During the active phase of MJO2 from Nov 22 to 28, wind speeds increase significantly (Fig. 3a and 3b). Two Kelvin waves can be seen clearly in both the observations and the 27km simulation (Fig. 3a), but they are absent from the 45km simulation. Air temperatures drop about 2-3 ^{o}C (Fig. 3c), relative humidities (Fig. 3d) increase about 30% from the suppressed phase and sea-level pressures (Fig. 3e) decrease to the lowest value during the simulation period. The short wave radiation also decreases substantially since convective clouds are increased during the active phase. Time-mean values from all variables show the 27-km simulation is outperform 45km simulation. The mean-values from the 27-km simulation are close to the observation, indicating the smaller biases compared to the 45km simulations.

Fig. 3. Daily mean surface variables at 0^o, 80.5^{o}E from RAMA and COAMPS simulations. (a) u-component and (b) v-component of surface wind. (c) surface temperature. (d) relative humidity. (e) shortwave radiation.

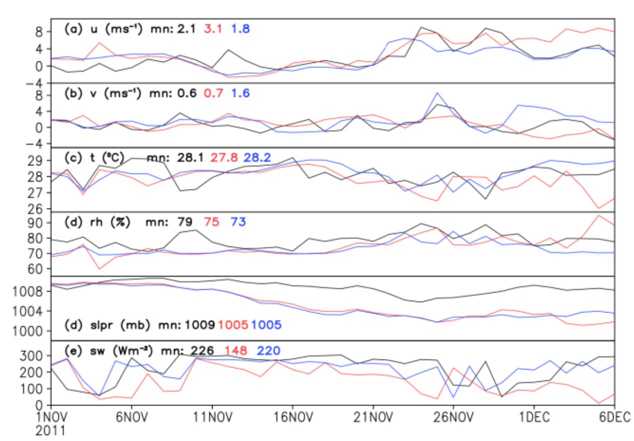

C. *Ocean temperature*

Mixed-layer depth (light blue lines in Fig. 4) is defined as the depth at which density increases by Δd above the surface value [11]. Δd is specified to be equivalent to the density increase produced by a 0.3 °C decrease in temperature from the surface value, but with the salinity held constant at the surface value. The top of the thermocline depth (black lines in Fig. 4) is defined as the depth at which temperature decreases by ΔT above the surface value. ΔT is specified to be 0.3 °C. The thickness of the barrier layer is defined as the isothermal layer below the mixed-layer [12]. The mixed-layer depth and the top of the thermocline are shallow, about 5 m and 10-20 m from RAMA observation and even shallower from the 27-km simulation during the suppressed phase from Nov 12 to 22. The deep mixed-layer in earlier November from MJO1 lasts longer in the model simulations than in the observation. The barrier layer during the suppressed phase is captured in the 27-km run but is not quite consistent with the 45-km run during this period. The rapid deepening of the mixed-layer produced by the strong westerly winds during the active phase from Nov 24 to 28 and the mixed-layer recovering trend after the active phase are consistent between the RAMA observation and the 27-km run. The barrier layer erosion by the strong winds during the active phase is also shown in both observation and the 27-km run.

Fig. 4. Ocean temperature at 0°, 80.5 °E from (a) COAMPS and (b) RAMA. The light blue solid line is the mixed layer depth and the black solid line is the top of thermocline depth.

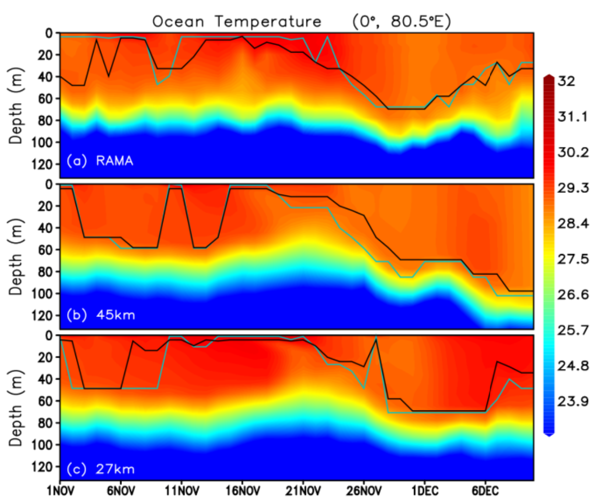

D. *Air-sea interaction*

The ocean warms during the suppressed phase due to the strong heat flux exerted on the ocean from the atmosphere and cools during the active phase of the MJO due to increased evaporation (latent heat flux) associated with strong westerly winds. The slow propagation of warm water is seen in the observation and simulations. However, the ocean water is too warm in the 45-km simulation (Fig. 5b) compared to the 27-km simulation (Fig. 5c) and the observation (Fig. 5a). ECMWF SSTs are warmer than RAMA SST (red dashed line) but both have similar warming and cooling phase before and after the active phase. The 45-km run shows maximum SST is larger and not in phase with the RAMA SST. The SST in both runs is colder than the RAMA SST during the cooling phase. However, the peak of the warm SST is closer both in timing and magnitude to the RAMA SST in the 27-km run than in the 45-km run and the ECMWF analysis. One issue with using the ECMWF analysis for verification is the 6-h output interval may not adequately capture the diurnal variation.

Fig. 5. Hovmöller diagrams of SST and surface heat flux (Wm^{-2}) averaged between 2.5°S and 2.5°N from (a) ECMWF analysis, (b) 45km and (c) 27km. The corresponding time series for SST at RAMA location are shown at right-hand side (the red dashed-line is SST for RAMA).

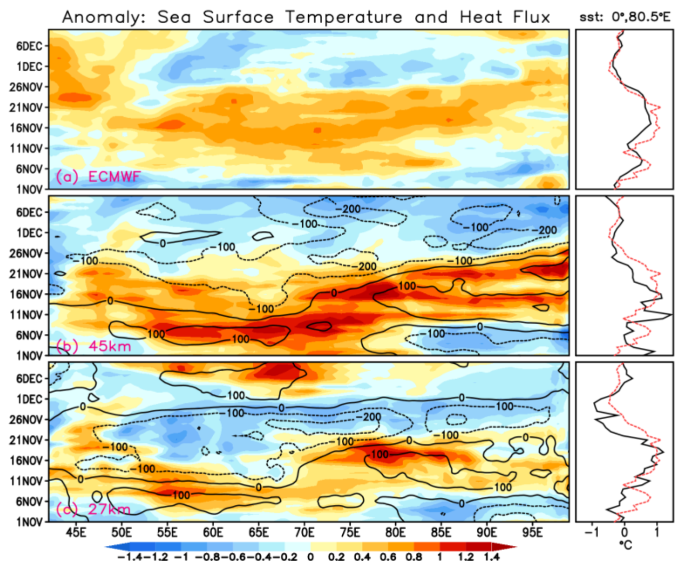

E. *Ocean Dynamical Feedback*

During the suppressed phase from Nov. 12 to 20 (Fig. 6a, 6d, and 6g), oceanic downwelling equatorial Rossby waves reflected by previous downwelling equatorial Kelvin waves at

Fig. 6. Anomalies of sea surface height (color shaded) and temperature (contour) during the suppressed (a, d and g), active (b, e and h) and post-suppressed (c, f and i) phases of the MJO2 from 45km (left column), 27km (middle column) and ECMWF analysis (right column). ONLY SST anomalies are available from the ECMWF.

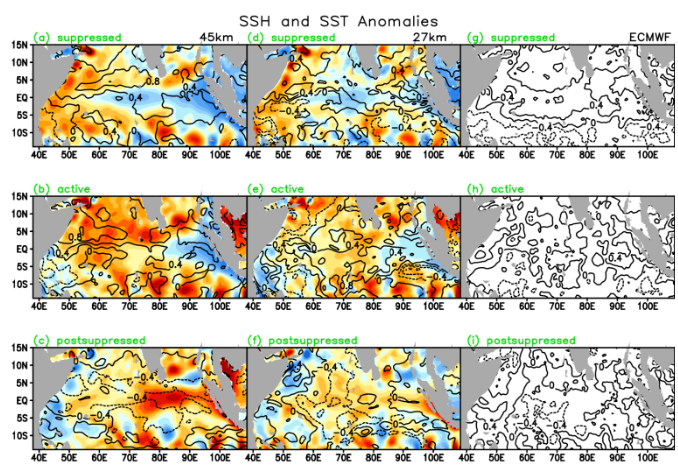

Sumatra are propagating westward across the Indian Ocean and arriving in the western Indian Ocean. The Rossby waves in the western Indian Ocean generate positive SST anomalies (Fig. 6a, 6d, and 6g), which create favorable condition for convective activity to develop and for initiation of MJO2. During the active phase from Nov. 24 to 28 (Fig. 6b, 6e, and 6h), conditions are more favorable for convection. After MJO2, downwelling equatorial Kelvin waves and Rossby waves are generated (Fig. 6c, 6f, and 6i).

Positive OLR anomalies in the eastern Indian Ocean (Fig. 7a, 7d and 7g) correspond to the formation of downwelling equatorial Rossby waves shown in Fig. 6a, 6d and 6g. Easterlies are dominant over the entire tropical Indian ocean during the suppressed phase. Negative OLR anomalies with strong westerlies show the convective phase of MJO2 (Fig. 7b, 7e and 7h). The oceanic condition shown in Fig. 6b, 6e and 6h have played a role in the enhancement of convective activity. Positive OLR anomalies in the eastern Indian Ocean during the postsuppressed phase (Fig. 7c, 7f, and 7i) create the downwelling equatorial Rossby waves shown in Fig. 6c, 6f and 6i.

Fig. 7. Anomalies of Outgoing longwave radiation (OLR, color shaded) and surface wind (vector) during the suppressed, active and post-suppressed phase of the MJO2 from 45km (left column), 27km (middle column) and ECMWF analysis with OLR observation (right column).

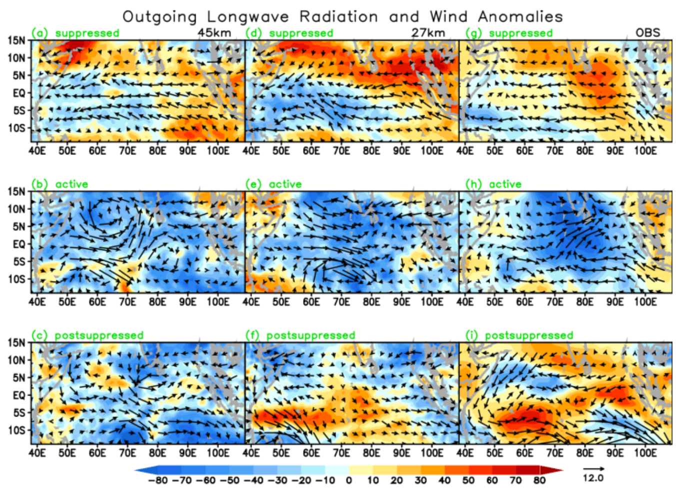

F. *Diurnal SST Amplitude*

The diurnal amplitude of SST is defined as a half difference between the maximum and minimum SST within 24 h [11]. Spatial pattern of diurnal SST amplitude during the suppressed phase from Nov. 12 to 20 from 45km and 27km runs show strong diurnal warming over the tropical Indian Ocean (Fig. 8a and 8d). This is due to weak wind speed (less than 2 ms^{-1}) over the area (Fig. 8b and 8e). Strong shortwave radiation south of 10 ^{o}S (Fig. 8b and 8e) does not correspond to strong diurnal warming due to the large wind speed over the same region (Fig. 8c and 8f). Weak wind conditions during the suppressed phase are mostly responsible for the observed large diurnal warming.

IV. SUMMARY

Regional extended-range simulations with two different horizontal resolutions are examined using the Navy's non-hydrostatic COAMPS modeling system in a two-way coupled mode for the DYNAMO time period of November to December 2011. Evaluation of the 61-day simulations indicates

Fig. 8. Mean diurnal SST amplitude (a and d), wind speed (b and e) and shortwave radiation averaged (c and f) during the suppressed phase from Nov. 12 to 20 from 45km (left column) and 27km (right column) simulations.

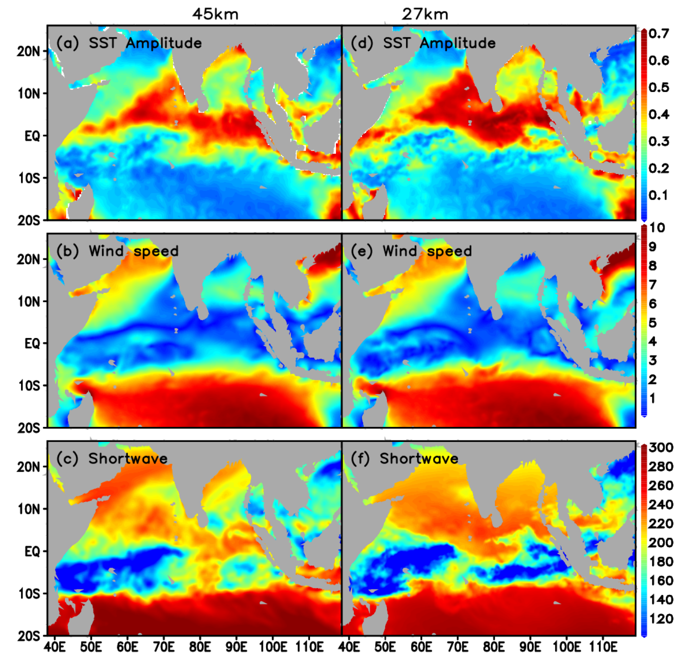

that the 27-km run provides much more accurate precipitation than the 45-km run. The 27-km run is able to simulate three MJOs during this period as shown in the TRMM observation. The initiation, propagation and characteristics of the MJOs are better captured when the model horizontal resolution is increased from 45 km to 27 km. Temporal variations of SST are in phase with surface heat flux, in which SST warms (cools) during the suppressed (active) phase through downward (upward) heat fluxes. Barrier layers that exist during the suppressed phase and erode during the active phase are consistent between the observation and the 27-km run. The extended-range simulations capture the propagation of oceanic downwelling equatorial Rossby waves, which provide favorable conditions for convective activity for initiation of the MJO. The model simulations are also able to capture the diurnal warming during the suppressed phase.

Further evaluation of the atmospheric component of the simulations (not shown) also show that even at these fairly coarse resolutions, these regional extended-range simulations are capable of capturing the main characteristics of the MJO. Due to limited computational resources, long-range high resolution runs are difficult to achieve.

ACKNOWLEDGMENT

This research is supported by the Office of Naval Research (ONR) Directed Research Initiative (DRI) Predictability of Seasonal and Intraseasonal Oscillations and partially supported by the ONR Litteral Air-sea processes DRI under program element 061153N. Computations were performed on the CRAY (Einstein) at the Navy DoD Supercomputing Resource Center (DSRC) at Stennis Space Center, Mississippi.

References

[1] R. Madden and P. Julian, "Detection of a 40-50 day oscillation in the zonal wind in the tropical Pacific," J. Atmos. Sci., vol 28, 702-708, 1971.

[2] C. Zhang, "Madden-Julian Oscillation," Reviews of Geophysics, vol 43, 1-36, 2005.

[3] R. M. Hodur, "The Naval Research Laboratory's Coupled Ocean/Atmosphere Mesoscale Prediction System (COAMPS)," Mon. Wea. Rev., vol 125, 1414-1430, 1997.

[4] P. J. Martin, "A description of the Navy Coastal Ocean Model version 1.0," NRL Rep. NRL/FR/7322-00-9962, Naval research Laboratory, Stennis Space Center, MS, 42 pp.

[5] J. A. Cummings and O. M. Smedstad, "Variational data assimilation for the global ocean," in Data Assimilation for atmospheric, oceanic and hydrological applications (vol. ii), S. K. Park and L. Xu, Eds. Springer Berlin Heidelberg, 2013, pp. 303-343.

[6] G. J. Huffman, et al., "The TRMM multisatellite precipitation analysis (TMPA): quasi-global, multiyear, combined-sensor precipitation estimates at fine scales," Mon. Wea. Rev., vol 8, 38-55, 2007.

[7] M. J. McPhaden, and Coauthors, "RAMA: The research moored array for African-Asian-Australian monsoon analysis and prediction," Bull. Amer. Meteor. Soc., vol 90, 459-480, 2009.

[8] B. W. Kerns, and S. S. Chen, "Equatorial dry air intrusion and related synoptic variability in MJO initiation during DYNAMO," Mon. Wea. Rev., vol 142, 1326-1343, 2014.

[9] W. Xu, and S. A. Rutledge, "Convective characteristics of the Madden-Julian Oscillation over the central Indian Ocean observed by shipborne radar during DYNAMO," J. Atmos. Sci., vol 71, 2859-2877, 2014.

[10] S. C. Peatman, A. J. Mattews, and D. P. Stevens, "Propagation of the Madden-Julian Oscillation through the Maritime Continent and scale interaction with the diurnal cycle of precipitation," Q. J. R. Meteorol. Soc., vol 140, 814-825, 2013.

[11] T. Shinoda, T. G. Jensen, M. Flatau, and S. Chen, "Surface wind and upper-ocean variability associated with the Madden-Julian Oscillation simulated by the coupled ocean-atmosphere mesoscale prediction system (COAMPS)," Mon. Wea. Rev., vol 141, 2290-2307, 2013.

[12] R. Lukas and E. Lindstrom, "The mixed layer of the western equatorial Pacific Ocean," J. Geophys. Res., vol 96, 3343-3357, 1991.